PAPER

Check for updates

Terbium-modified two-dimensional zirconium-based metal–organic frameworks for photoluminescence detection of nitrite†

You-Liang Chen, Cheng-Hui Shen, Chi-Wei Huang and Chung-Wei Kung [iD] *

In this study, spatially isolated terbium ions are post-synthetically installed on a two-dimensional (2D) water-stable zirconium-based metal–organic framework (MOF), ZrBTB (BTB = 1,3,5-tri(4-carboxyphenyl) benzene), and the loading of installed terbium ions is adjusted by tuning the synthetic temperature of the post-synthetic process. The crystallinity, porosity, morphology, chemical state, and terbium loading of the obtained materials are characterized. Tb-modified MOFs synthesized at various temperatures were subjected to photoluminescence tests in aqueous environments, and the energy transfer from the BTB linkers to the installed terbium sites is highly tunable by adjusting the temperature for installing terbium. Since the photoluminescence of the installed terbium sites can be quenched by the nitrite ions present in the solution, as a demonstration, the terbium-incorporating MOFs are applied for nitrite quantification by utilizing the Stern–Volmer equation; a high Stern–Volmer constant of 472 000 M^{-1} and a low limit of detection of 0.08 μM can be achieved.

Design, System, Application

Since the direct synthesis of lanthanide-based MOFs with both high porosity and high chemical stability in water is still challenging, post-synthetic modification (PSM) of lanthanide ions into another highly porous and chemically robust MOF, *e.g.*, zirconium-based MOFs (Zr-MOFs), becomes an attractive option, especially for applications in aqueous media. Compared to traditional 3D MOFs, 2D MOF sheets exhibit the advantages of more external surface area and ease of being dispersed in solvents. However, to date there is no study reporting the PSM of luminescent lanthanide on 2D Zr-MOFs. In this work, we demonstrated the use of PSM to immobilize spatially separated terbium ions on the unsaturated hexa-zirconium nodes of a 2D Zr-MOF. Under excitation, the energy transfer occurred from the MOF linkers to the installed terbium sites through the "antenna effect", which could significantly amplify the photoluminescence of terbium. The findings here open up opportunities for utilizing such water-stable and porous 2D Zr-MOF sheets as a platform to post-synthetically install various luminescent metal ions with tunable loadings for a range of sensing and photocatalytic applications in aqueous solutions in future studies.

Introduction

As an emerging subcategory of porous materials, luminescent metal–organic frameworks (LMOFs) have attracted considerable attention in the past two decades.[1,2] The strong linkages between metal-ion clusters and organic linkers construct a well-crystallized and extended framework,[3,4] which offers several fascinating advantages, such as the ease of transporting the analyte to the active sites in the framework for sensing applications and the facile diffusion of reagents during photocatalysis.[5,6] Luminescent centers in a robust framework cause stronger emission owing to the effective reduction of non-radiative energy loss.[5,7] In

addition, structural tunability and adjustable luminescent features can be achieved through the selection of metal-based nodes and organic linkers.[8,9] These intriguing benefits make LMOFs unique platforms for various applications including chemical sensing,[5,10] imaging,[11] light harvesting,[12,13] and photocatalysis.[6]

Among numerous reported LMOFs, lanthanide-based metal–organic frameworks (LnMOFs) possess the distinctive advantages of narrow-line emission, little influence from the environment, and diverse luminescent features;[14,15] these characteristics result in the use of LnMOFs in numerous applications especially in luminescent chemical sensing.[15,16] In addition, the issue of a low molar extinction coefficient for most lanthanide-based materials can be overcome by selecting chromophoric organic linkers that induce energy transfer to lanthanide, which is known as the "antenna effect".[17–19] However, it is still challenging to synthesize

Department of Chemical Engineering, National Cheng Kung University, Tainan City, 70101, Taiwan. E-mail: cwkung@mail.ncku.edu.tw

LnMOFs with high porosity and design the desired structure owing to variable coordinating characteristics of lanthanide ions.[14,20–22]

Post-synthetic modification (PSM), which performs chemical modification on the as-synthesized MOF without changing the structure of the scaffold, may provide an opportunity to tackle the aforementioned challenge.[23–25] The installation of spatially dispersed lanthanide sites within a selected MOF can be achieved by PSM, and the resulting material not only preserves its original framework structure, but also exhibits the expected luminescence.[26,27] However, most MOFs suffer from poor chemical stability in aqueous media, which strongly limits their applications in water-containing environments.[3,4,28] Fortunately, the MOFs constructed from group 4 metal-based nodes, *e.g.*, zirconium-based MOFs (Zr-MOFs), possess the features of exceptional chemical stability in water, high porosity, and tunable intra-framework chemical functionality.[3,29–32] It is thus anticipated that Zr-MOFs can serve as ideal platforms for PSM and further expand the usefulness of lanthanide-based materials in various applications, especially in aqueous media. Several recent studies have proven that the PSM of lanthanide in Zr-MOFs is feasible. For example, in an early study published in 2019, Zhao and coworkers reported the successful incorporation of spatially separated terbium ions in a three-dimensional (3D) Zr-MOF, MOF-808, for luminescence sensing in aqueous media.[33] Similar approaches were also used to install lanthanide ions in a range of Zr-MOFs.[34–36]

However, most published studies reporting luminescent MOFs to date focused on 3D MOF structures. Compared to 3D MOFs, two-dimensional (2D) MOF structures provide the advantages of a more exposed external surface area, extremely high aspect ratio with extended lateral dimensions, and colloidal nature.[37,38] These superiorities result in the better performances of 2D MOFs compared to their 3D counterparts in numerous applications including catalysis,[39,40] light harvesting,[41] and especially luminescent chemical sensing; the readily available contact between the 2D MOF sheet and the target analyte enables a more rapid and sensitive detection.[42,43] Among the limited number of 2D Zr-MOFs, a six-connected Zr-BTB (BTB = 1,3,5-tri(4-carboxyphenyl)benzene) has attracted great attention due to its distinctive stability in water, ultrathin nanosheets, and chemical functionality on unsaturated hexa-zirconium clusters.[44,45] It is worth mentioning that the light-harvesting behavior of BTB has been investigated in the ZrBTB framework.[46] We thus reasoned that by installing lanthanide sites on the water-stable ZrBTB sheets, the luminescent intensity of lanthanide should be amplified by means of the energy transfer from the BTB linkers, which is beneficial for luminescence sensing in aqueous media. However, to date there is no study reporting the installation of lanthanide in 2D Zr-MOFs.

As one of the commonly used lanthanide elements, terbium (Tb) has been widely applied for nitrite sensing.[47] The dynamic quenching of terbium-based luminescence is achieved by the energy transfer from terbium ions to nitrite owing to the slightly higher triplet energy level of terbium ions ($20\,500\ cm^{-1}$) than that of nitrite ($19\,084\ cm^{-1}$).[47,48] Such a quenching mechanism occurring in various 3D MOF-based materials, *e.g.*, Tb-based MOF and Tb-incorporated indium-based MOF, has been utilized for nitrite sensing.[47,48] However, a study on such sensing processes occurring in 2D MOFs has not been reported yet.

In this study, terbium ions were immobilized on the unsaturated hexa-zirconium nodes of ZrBTB by a solution-phase PSM process (see Fig. 1). It has been reported that BTB can serve as the antenna to induce the energy transfer to terbium ions.[49] Therefore, it is anticipated that a similar energy-transfer behavior should be observed between the well-aligned BTB linkers in MOF nanosheets and the installed terbium ions. As demonstrated here, the obtained terbium installed ZrBTB was applied for the photoluminescence detection of nitrite.

Experimental

1. Chemicals

All chemicals including zirconium(IV) chloride anhydrous ($ZrCl_4$, Acros Organics, 98%), benzoic acid (BA, Sigma-Aldrich, 99.5%), 1,3,5-tri(4-carboxyphenyl)benzene (H_3BTB, Alfa Aesar, 97%), *N,N*-dimethylformamide (DMF, ECHO Chemical Co, Ltd., Taiwan, ≥99.8%), dimethyl sulfoxide (DMSO, Duksan Pure Chemicals, 99%), hydrochloric acid (HCl, J. T. Baker, 36.5–38.0%), acetone (ECHO Chemical Co, Ltd., Taiwan, 98%), ethanol (ECHO Chemical Co, Ltd., Taiwan, 99.5%), terbium(III) acetate hydrate (Alfa Aesar, 99.9%), dimethyl sulfoxide-d_6 (DMSO-d_6, Sigma-Aldrich, 99.9 atom% D), sulfuric acid-d_2 solution (D_2SO_4, Sigma-Aldrich, 96–98 wt% in D_2O, 99.5 atom% D), sodium sulfate (Na_2SO_4, Sigma-Aldrich, ≥99.0%), sodium chloride (NaCl, Sigma-Aldrich, 99%), sodium nitrite ($NaNO_2$, Alfa Aesar, 98%), magnesium chloride hexahydrate ($MgCl_2 \cdot 6H_2O$, Sigma-Aldrich, 98%), zinc chloride ($ZnCl_2$, Sigma-Aldrich, ≥98%), calcium chloride ($CaCl_2$, J. T. Baker, ≥89%), sodium nitrate ($NaNO_3$, Alfa Aesar, 98%), sodium perchlorate ($NaClO_4$, Alfa Aesar, 98%), sodium bicarbonate ($NaHCO_3$, Honeywell Fluka, 99.7%), sodium bromide (NaBr, Sigma-Aldrich, 98%), ammonium fluoride (NH_4F, Alfa Aesar, 98%), potassium carbonate (K_2CO_3, Sigma-Aldrich, 98%), hydrogen peroxide solution (H_2O_2, Honeywell Fluka, 30–31%), sulfuric acid (H_2SO_4, Honeywell Fluka, 95.0–98.0%), and nitric acid (HNO_3, Honeywell Fluka, ≥65%) were used without purification. Deionized (DI) water was used as the water source throughout the whole work.

2. Synthesis of ZrBTB

The synthetic protocol of ZrBTB followed previously published studies, with the use of benzoic acid as the modulator.[44,50] First, 100 mg of H_3BTB, 100 mg of $ZrCl_4$, 6 g of benzoic acid, 5 mL of DI water, and 30 mL of DMF were added into a DURAN® glass laboratory bottle (100 mL), and

This journal is © The Royal Society of Chemistry and IChemE 2023

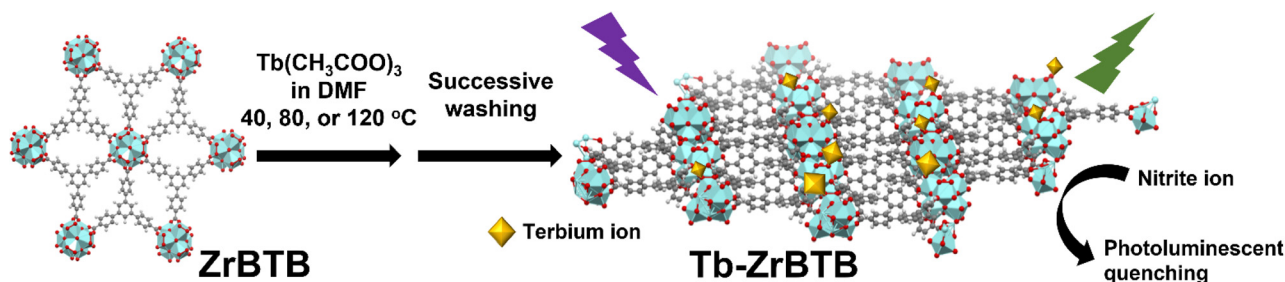*Mol. Syst. Des. Eng.*, 2023, **8**, 330–340 | 331

Fig. 1 Schematic representation of the terbium installed on a 2D ZrBTB by using post-synthetic modification for use in photoluminescence nitrite sensing. Cyan: Zr; red: O; grey: C.

the bottle was sealed by a polytetrafluoroethylene (PTFE)-lined cap. The mixture was sonicated for 10 min to obtain a colorless and homogeneous solution, and then kept at 120 °C in an oven for 48 h. After cooling the mixture to room temperature, the white precipitate was washed with 35 mL of fresh DMF three times by centrifugation to remove the excessive reagents. The MOF powder was then obtained after the solvent exchange with acetone three times, with immersing periods of 2 h, overnight, and 2 h in between, respectively. The obtained powder was activated in a vacuum oven at 80 °C overnight, and the sample was named as "BA-ZrBTB".

To remove the coordinated benzoate from the hexa-zirconium nodes of BA-ZrBTB, the heating process in a HCl/DMF mixture was usually used in early studies.[44] However, coordinated formate ions on hexa-zirconium nodes originating from the decomposition of DMF may still be present after such an activation process, resulting in the small amount of available $-OH/-OH_2$ groups on the nodes.[51] A more effective strategy to substitute the coordinated benzoate with $-OH/-OH_2$ ligands should be the use of DMF-free solutions to remove the modulator.[51] Following this approach, the following experiments were conducted. 50 mg of BA-ZrBTB was dispersed in 15 mL of DMSO and 0.6 mL of 8 M HCl (aq), and the mixture was kept at room temperature for 18 h. Thereafter, the mixture was washed with 15 mL of fresh DMSO four times by centrifugation over the course of 8 h, and solvent exchange with acetone was then performed three times as mentioned previously. The resulting powder was activated at 80 °C under vacuum overnight, and the activated "ZrBTB" was thus obtained.

3. Synthesis of Tb-ZrBTB

For the installation of terbium in ZrBTB, post-synthetic modification (PSM) was utilized at various temperatures.[33] Generally, 146 mg of terbium(III) acetate hydrate was dissolved in 12 mL of DMF by sonication to obtain a colorless solution. Thereafter, 30 mg of ZrBTB powder was dispersed in the obtained solution, and the mixture was kept at 40, 80, or 120 °C in an oven for 12 h. The resulting solid was washed with 12 mL of fresh DMF three times by centrifugation to completely remove the residual terbium precursor from the

Tb-decorated MOF solid. Solvent exchange with 12 mL of acetone three times and activation under vacuum at 80 °C were then performed, similar to the procedure mentioned previously for the synthesis of BA-ZrBTB and ZrBTB. The white products obtained by the PSM process at 40, 80, and 120 °C were named as "Tb-ZrBTB-40", "Tb-ZrBTB-80", and "Tb-ZrBTB-120", respectively.

4. Photoluminescence experiments

All photoluminescence experiments were carried out at room temperature with the excitation wavelength of 310 nm,[46] and the experimental details are described as follows. Accurately weighted 4.0 mg of Tb-decorated MOF powder was first uniformly dispersed in 10 mL of ethanol by sonication. Thereafter, 1.5 mL of the resulting mixture was mixed with 1.5 mL of DI water. The reason for choosing the water–ethanol cosolvent system will be discussed later. After vigorous shaking for 15 s, the suspension was subjected to photoluminescence measurements to record the emission spectra. In addition to the photoluminescence tests of Tb-decorated MOFs, 4.0 mg of terbium(III) acetate hydrate dissolved in 20 mL of the same water–ethanol cosolvent, and 4.0 mg of BA-ZrBTB evenly dispersed in the aforementioned terbium acetate solution, were also subjected to photoluminescence measurements for comparison in order to probe the effective energy transfer between the BTB linkers and the installed terbium sites within the Tb-decorated MOFs.

5. Detection of nitrite

The photoluminescence sensing of nitrite was performed by conducting the following experiments.[47] At the beginning, 4.0 mg of Tb-ZrBTB-120 was dispersed in 10 mL of ethanol by sonication. Then, 1.5 mL of the obtained suspension was added into 1.5 mL of the aqueous solution containing a certain concentration of nitrite. After vigorous shaking for 15 s, the photoluminescence spectrum of the resulting mixture was collected at the excitation wavelength of 310 nm. The calibration line for nitrite detection was obtained by recording the emission intensity at 543 nm in the presence of various concentrations of nitrite in the tested samples. It should be noted that the concentration of nitrite here is

332 | Mol. Syst. Des. Eng., 2023, **8**, 330–340

This journal is © The Royal Society of Chemistry and IChemE 2023

defined as the final concentration in the 3 mL mixture. The Stern–Volmer equation was then utilized to acquire the linear relationship,[47]

$$\frac{I_0}{I} = 1 + K_{sv}[NO_2^-] \qquad (1)$$

where I_0 is the emission intensity of the sample without adding nitrite, I is the emission intensity of the sample at a given concentration of nitrite ($[NO_2^-]$), and K_{sv} represents the Stern–Volmer constant.

6. Selectivity tests

The interference of various cations and anions in the photoluminescence sensing process was investigated by the following steps. 4.0 mg of Tb-ZrBTB-120 was dispersed in 10 mL of ethanol by sonication, and 1.5 mL of the obtained suspension was mixed with 1.5 mL of the aqueous solution containing 20 μM of the selected interferent. It should be noticed that the final concentration of interferents in the tested solution is 10 μM. Photoluminescence spectra of the samples were then collected after vigorous shaking.

7. Instrumentation

The energy-dispersive X-ray spectroscopic (EDS) data of ZrBTB and Tb-ZrBTB-120 were collected using a scanning electron microscope (SEM, Hitachi SU8010). Pt was sputtered on the samples before EDS measurements. The morphologies of all the materials were probed using a transmission electron microscope (TEM, Hitachi H7500). The crystallinity of the samples was investigated using a powder X-ray diffractometer (PXRD, RIGAKU Ultima IV). Fourier-transform infrared (FTIR) spectra were collected by using a Nicolet 6700 (Thermo Fisher Scientific). Nitrogen adsorption–desorption isotherms of the samples were measured with an ASAP 2020 (Micromeritics). High-resolution transmission electron microscopy (HR-TEM) images and corresponding EDS elemental mapping data were collected using a JEM-2100F (JEOL) at the operating voltage of 200 kV. X-ray photoelectron spectroscopy (XPS) of ZrBTB and Tb-ZrBTB-120 was performed on a Theta Probe (Thermo Scientific) equipped with a microfocused electron gun, a multi-position aluminum anode, and a monochromated X-ray source. All XPS spectra were corrected by referencing the C 1s peak to 284.8 eV. Inductively coupled plasma-optical emission spectrometry (ICP-OES) measurements were conducted to detect the elemental contents of all the materials by using a JY 2000-2 ICP-OES spectrometer (Horiba Scientific). The preparation of ICP-OES samples was described as follows. 0.75 mL of sulfuric acid, 0.25 mL of 30% H_2O_2 aqueous solution, and around 1 mg of the MOF-based powder were mixed in a microwave vial (2–5 mL, Biotage). Thereafter, the vial was crimped and heated at 100 °C in an oil bath for 24 h, and the resulting colorless solution was diluted to 40 mL with 3 wt% of HNO_3 aqueous solution. For quantifying the exact amount of zirconium in a certain amount of the MOF

sample, 4.0 mg of the MOF-based powder was accurately weighted in a microwave vial and was subjected to similar digesting and diluting procedures mentioned above; the obtained 40 mL sample was subjected to ICP-OES measurements. Photoluminescence spectra were measured using a FluoroMax® spectrometer (HORIBA Scientific). The ^1H nuclear magnetic resonance (NMR) spectra of all samples were measured with a Bruker AVANCE 600NMR spectrometer. For the preparation of NMR samples, around 0.5 mg of the MOF-based solid was dissolved in a few drops of D_2SO_4, and 0.7 mL of DMSO-d_6 was added to dilute the solution. The obtained solution was then sonicated for 20 min before being filled into the NMR tube. All the washing and solvent-exchange procedures in this study were conducted by using a Heraeus™ Megafuge™ 16 centrifuge (Thermo Fisher Scientific) with a TX-400 rotor at the rotating speed of 5000 rpm.

Results and discussion

1. Material characterization

The exposed aqua and hydroxyl groups on hexa-zirconium nodes of Zr-MOFs provide the reactive grafting sites to install uniformly spaced metal ions by PSM.[52,53] We thus reasoned that the 6-connected Zr-BTB with six pairs of terminal –OH/–OH$_2$ groups on each node should be an attractive platform for installing terbium. However, since ZrBTB was synthesized by using benzoic acid as the modulator, the removal of coordinated benzoate to maximize the number of accessible –OH/–OH$_2$ groups on the Zr$_6$ nodes prior to terbium installation is necessary.[50] In this work, protonation of benzoate-grafted ZrBTB (BA-ZrBTB) was accomplished by using the DMSO/HCl treatment,[51] and the successful removal of coordinated benzoate was confirmed by solution-phase ^1H NMR spectra. As shown in Fig. S1,† there are on average 3.2 benzoates coordinated on each node of BA-ZrBTB, and all benzoates were completely removed after the protonation process (see Fig. S1 and corresponding detailed discussion in the ESI†). Thus, with the accessible –OH/–OH$_2$ groups present on its hexa-zirconium nodes, the obtained ZrBTB was subjected to further installation of terbium at various temperatures. The ^1H NMR spectra of all digested Tb-installed MOFs were also collected (see Fig. S2 and corresponding detailed discussion in the ESI†). The coordinated acetate and a trace amount of residual formate, which came from the PSM process and the decomposition of DMF during the synthesis,[54] respectively, are present in all the materials.

PXRD patterns of BA-ZrBTB, ZrBTB, Tb-ZrBTB-40, Tb-ZrBTB-80, and Tb-ZrBTB-120 are shown in Fig. 2. Both PXRD patterns of BA-ZrBTB and ZrBTB show two main diffraction peaks located at 5.2 and 8.9 degrees, which are attributed to the crystal planes of (100) and (110) in ZrBTB, respectively.[45,50] As revealed in Fig. 2, the diffraction peaks in the patterns of all the MOF-based materials also agree well with those in the simulated pattern of ZrBTB reported
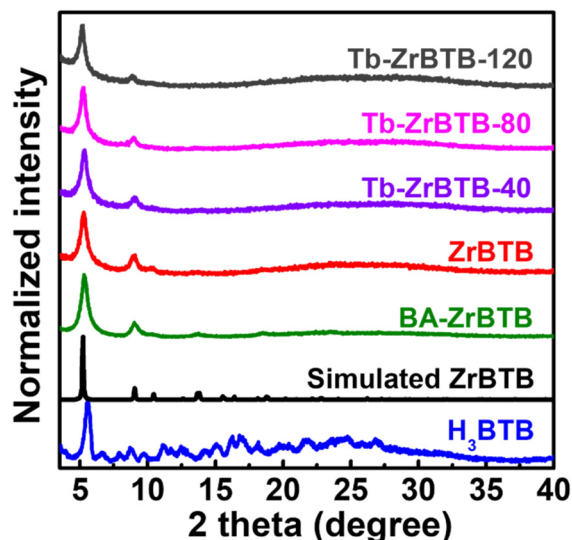
This journal is © The Royal Society of Chemistry and IChemE 2023

Mol. Syst. Des. Eng., 2023, **8**, 330–340 | 333

Fig. 2 PXRD patterns of H_3BTB, BA-ZrBTB, ZrBTB, Tb-ZrBTB-40, Tb-ZrBTB-80, and Tb-ZrBTB-120. The simulated pattern of ZrBTB is also shown.

Fig. 3 HR-TEM images of Tb-ZrBTB-120 at (a) low magnification and (b) high magnification. Corresponding EDS elemental mapping data for (d) terbium and (e) zirconium recorded in the rectangular region shown in (c).

previously.[45] The PXRD pattern of the H_3BTB linker is also shown in Fig. 2, which possesses multiple peaks in the high-angle region. As these peaks are not present in the PXRD patterns of all MOF-based materials synthesized here, it indicates that the residual H_3BTB linker has been mostly removed from the MOF during the synthetic process. It should be noticed that the as-synthesized Zr-BTB is isostructural with the reported 2D Zr-MOFs, UMCM-309a and NUS-8 (Zr),[45,55] according to the PXRD results. After the installation of terbium at various temperatures, both diffraction peaks can still be observed in all the three PXRD patterns, which suggests that the crystallinity of Zr-BTB can be well preserved after the installation of terbium.

EDS spectra of Tb-ZrBTB-120 and ZrBTB are shown in Fig. S3(a) and (b),† respectively. The signals of both zirconium and terbium were detected in Tb-ZrBTB-120, verifying the successful installation of terbium in ZrBTB by PSM. In addition, the presence of chloride in ZrBTB may be attributed to the use of HCl for removing the coordinated benzoate.[51] From the EDS data shown in Fig. S3,† there are on average 2.3 chloride ions on each hexa-zirconium node of Zr-BTB, and the loading of chloride becomes negligible after the installation of terbium. TEM images were further collected to investigate the morphologies of the materials. As shown in Fig. S4,† the flower-shape morphology constructed with ultrathin 2D layers can be observed in the images of all the five materials, indicating that there is no morphological change after both the removal of benzoate and the installation of terbium at various temperatures; this morphology is also consistent with that of ZrBTB reported previously.[56] Representative HR-TEM images of Tb-ZrBTB-120 are shown in Fig. 3(a and b). It is found that the material is composed of nanosheets with a smooth and clean surface without any particles on the layer, indicating that there is no
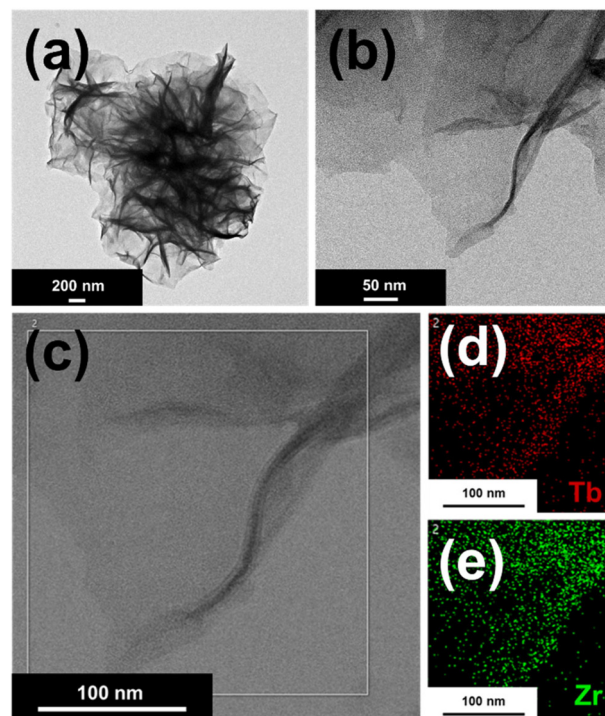
aggregation of the installed terbium generated during the PSM. EDS elemental mapping data of Tb-ZrBTB-120 also revealed the uniform distributions of both zirconium and terbium on the 2D nanosheet (Fig. 3(c–e)). These findings clearly suggest that uniformly spaced terbium ions immobilized on the nodes of ZrBTB can be synthesized by PSM without producing aggregated terbium nanoparticles. The similar PSM was also performed in another 3D Zr-MOF in previous work.[33]

ICP-OES measurements were further performed to quantify the loadings of terbium in Tb-installed materials. The results show that the average atomic loadings of terbium per hexa-zirconium node in Tb-ZrBTB-40, Tb-ZrBTB-80, and Tb-ZrBTB-120 are 0.8, 2.0, and 3.3, respectively. This finding implies that the controllable loading of terbium in ZrBTB can be achieved by simply adjusting the temperature of PSM. At a higher temperature during the solution-phase PSM, the deprotonation of the terminal $-OH/-OH_2$ group may become easier, which results in more terbium ions coordinating on the hexa-zirconium nodes after the PSM process.

FTIR spectra of ZrBTB and the H_3BTB linker were further collected. As shown in Fig. S5,† three characteristic signals located at 1610, 1543, and 1413 cm^{-1} can be observed in both spectra, which confirms the presence of O–C–O and aromatic C=C bonds in ZrBTB.[57] In addition, two strong peaks located at 1704 and 1252 cm^{-1} in the spectrum of H_3BTB, which represent the C=O vibrations and C–OH bending of the free carboxylic acid, respectively,[58] become much weaker in the
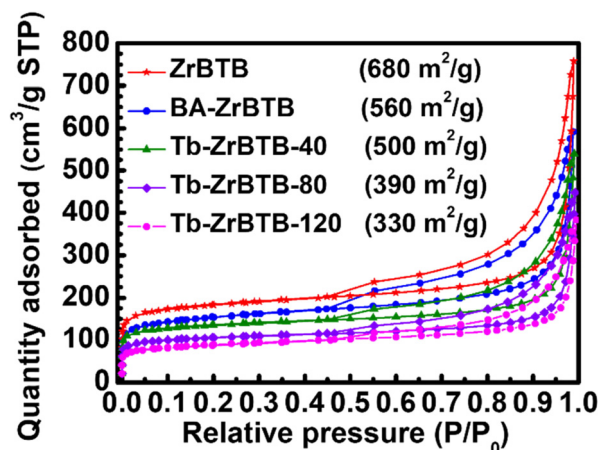
Fig. 4 Nitrogen adsorption–desorption isotherms of ZrBTB, BA-ZrBTB, Tb-ZrBTB-40, Tb-ZrBTB-80, and Tb-ZrBTB-120. The calculated BET surface area is also shown.

spectrum of ZrBTB. This finding indicates that the presence of free uncoordinated H_3BTB linkers in ZrBTB is negligible, which agrees with our PXRD data.

Nitrogen adsorption–desorption isotherms of all the MOF-based materials were collected at 77 K to investigate their porosities. As shown in Fig. 4, all the five isotherms possess a sharp gas uptake at low relative pressures and a remarkable gas uptake with a hysteresis loop in the region of high relative pressure, which correspond to the micropores and the interspace between stacked 2D MOF sheets, respectively; these characteristics agree well with those of ZrBTB reported previously.[50,59] BA-ZrBTB possesses a Brunauer–Emmett–Teller (BET) surface area of 560 m^2 g^{-1}, and its surface area increases to 680 m^2 g^{-1} after the removal of benzoate; these findings also agree well with the reported characteristics of BA-ZrBTB and ZrBTB.[50,56] The BET surface areas of Tb-ZrBTB-40, Tb-ZrBTB-80, and Tb-ZrBTB-120 decrease to 500, 390, and 330 m^2 g^{-1}, respectively, but the typical features of ZrBTB are still preserved in the corresponding isotherms, verifying that the major pores of the three Tb-installed MOFs are not clogged. Density functional theory (DFT) pore size distributions of the materials were then calculated from these isotherms. As shown in Fig. S6,† all the five materials show the main pore size centered at around 1.2 nm, which is consistent with the pore size of ZrBTB according to its crystal structure.[44,55]

XPS spectra of ZrBTB and Tb-ZrBTB-120 were further collected to investigate the chemical states of terbium and zirconium. As shown in Fig. 5(a), four well-defined peaks can be found in the XPS spectrum of Tb-ZrBTB-120 in the Tb 3d region. The two peaks located at the binding energy of 1241 eV and 1276 eV are the characteristic peaks of Tb^{3+} in $3d_{5/2}$ and $3d_{3/2}$ regions, respectively,[34] and the peaks centered at 1249 eV and 1283 eV correspond to Tb^{4+} in $3d_{5/2}$ and $3d_{3/2}$ regions, respectively.[34,60] The XPS data here suggest that the installed Tb ions in Tb-ZrBTB-120 possess the mixed oxidation states of Tb^{3+} and Tb^{4+}. XPS spectra of ZrBTB and
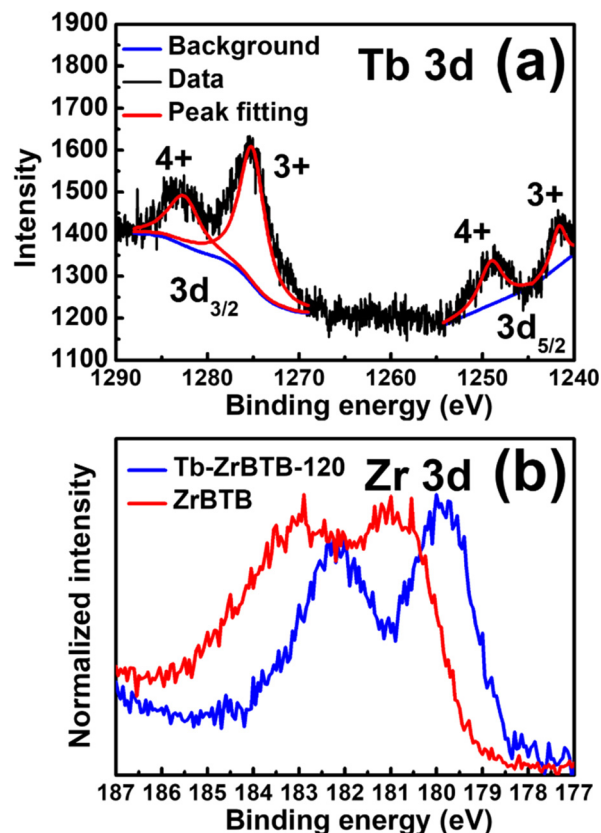

Fig. 5 XPS spectra of (a) Tb-ZrBTB-120 in the region of Tb 3d, and (b) Tb-ZrBTB-120 and ZrBTB in the Zr 3d region.

Tb-ZrBTB-120 in the Zr 3d region were also collected to probe the interaction between the installed metal ions and the hexa-zirconium nodes of Zr-MOFs.[54,61] As shown in Fig. 5(b), the Zr 3d peaks of Tb-ZrBTB-120 exhibit a negative shift of around 0.9 eV compared to those of ZrBTB. This result may be ascribed to the lower electronegativity of terbium than that of zirconium,[62] which makes the zirconium-based nodes more electron-rich after the installation of terbium; this finding suggests the successful installation of terbium on the nodes of ZrBTB by the PSM process.

Since Tb^{4+} ions are present in Tb-ZrBTB-120, it is crucial to identify if the terbium ions partially replaced the Zr^{4+} ions in the hexa-zirconium nodes of the MOF or not, as such post-synthetic metal substitutions between other group (iv) metal ions and Zr-MOFs have been reported previously.[63,64] According to the literature as well as our own EDS result, the chemical formula of ZrBTB after the removal of coordinated benzoate was determined as $Zr_6O_4(OH)_4(BTB)_2(OH)_{3.7}(H_2O)_{8.3}Cl_{2.3}$ (molecular weight (MW) = 1842).[51,56] After the installation of terbium at 120 °C, no chloride ions are left in Tb-ZrBTB-120, and there are on average 3.3 terbium ions on each hexa-zirconium node according to our ICP-OES data. In addition, eight acetate ions from the terbium precursor are present on each node (see Fig. S7†), which should be coordinated on the installed terbium ions or directly coordinated on the node *via* solvent-assisted ligand

incorporation (SALI) occurring during the PSM process.[65] By assuming that the metal substitution in hexa-zirconium nodes did not occur and each terbium ion bridged between two oxygen atoms of one terminal –OH/–OH_2 pair, the chemical formula of Tb-ZrBTB-120 can be proposed as Zr_6-$O_4(OH)_4(BTB)_2(TbOOH)_{3.3}(CH_3COO)_8$ (MW = 2654). According to these chemical formulas and corresponding MW, the ratio between the mass loading of zirconium in ZrBTB and that in Tb-ZrBTB-120 can be calculated to be 1.44, and this ratio should further increase, if the partial substitution of metal ions occurred in the hexa-zirconium nodes during the PSM. We then experimentally quantified the amounts of zirconium in 4.0 mg of the accurately weighted ZrBTB and Tb-ZrBTB-120 by ICP-OES (see the Experimental section), and the zirconium concentrations of the resulting ICP-OES samples are 27.8 ppm and 19.9 ppm, respectively. The obtained ratio is 1.4, which agrees well with the ratio calculated by assuming no metal substitution. The finding here suggests that all terbium ions in Tb-ZrBTB-120 are coordinated on the nodes of ZrBTB without replacing the zirconium ions in the nodes. The possible binding modes of terbium ions grafted on the hexa-zirconium nodes may be similar to that of other metal ions grafted on the nodes of 3D Zr-MOFs reported previously.[53] The terbium ion may be grafted between two oxygen atoms originating from one terminal –OH/–OH_2 pair of the node or coordinated on one oxygen atom originating from the terminal –OH or –OH_2 group.[53]

2. Photoluminescence test

It has been reported that the photoluminescent intensity of terbium cations can be significantly amplified through the energy transfer from the organic sensitizer incorporated in the framework, which is known as the "antenna effect".[7] It is thus anticipated that the photoluminescence of terbium installed in ZrBTB should be enhanced with the help of the spatially adjacent BTB linker. Emission spectra of various MOF-based materials dispersed in the cosolvent of water and ethanol (1 : 1) with a concentration of 0.2 mg solid per mL were collected under an excitation of 310 nm. As shown in Fig. 6(a), a board emission peak located at around 370 nm, which originates from the BTB linkers,[66] can be observed in all the emission spectra. After the installation of terbium, all the three Tb-installed materials show three narrow emission peaks located at around 488, 543, and 582 nm in their emission spectra; these peaks are consistent with the typical photoluminescent characteristics of terbium.[33,34] It should be noticed that with increasing temperature of PSM to install more terbium ions in ZrBTB, the emission of BTB significantly decreases, and the photoluminescent intensity of terbium is amplified. The finding here implies the energy transfer from the BTB linkers of ZrBTB to the installed terbium. Tb-ZrBTB-120 with the strongest photoluminescence of terbium was thus selected for the following experiments. It should be noticed that for the emission of terbium at 543 nm, the maximum
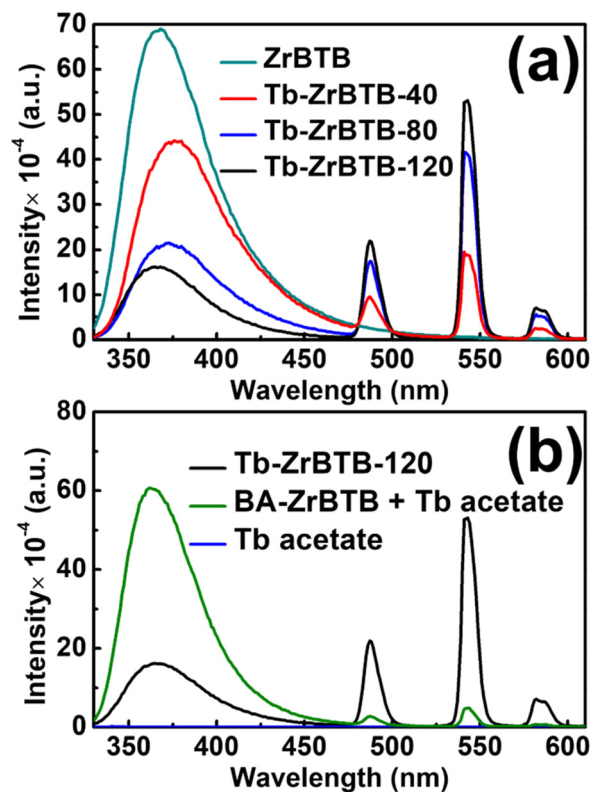

Fig. 6 Emission spectra of (a) ZrBTB, Tb-ZrBTB-40, Tb-ZrBTB-80, and Tb-ZrBTB-120, and (b) Tb-ZrBTB-120, terbium acetate solution, and BA-ZrBTB dispersed in the terbium acetate solution. Excitation at 310 nm was used to collect all spectra, and each solution is composed of water and ethanol (v : v = 1 : 1). The concentration of the MOF-based solid dispersed in the solutions and the concentration of dissolved terbium acetate are both 0.2 mg mL^{-1}.

excitation wavelength of Tb-ZrBTB-120 was confirmed to be 310 nm (Fig. S8†), which is the typical excitation wavelength of BTB.[46]

To further investigate the energy-transfer behavior from the BTB linker of ZrBTB to the installed terbium, the emission spectra of the solution solely containing the dissolved terbium precursor and the same solution with dispersed BA-ZrBTB were collected. It should be noted that the use of BA-ZrBTB here is to avoid any installation of terbium on the dispersed MOF during the photoluminescence test. As shown in Fig. 6(b), compared to the dispersed Tb-ZrBTB-120, the terbium acetate solution shows negligible emission, which indicates that the energy transfer from the BTB linkers is necessary to achieve the remarkable photoluminescent emission of terbium. Moreover, with both dispersed BA-ZrBTB and dissolved terbium acetate coexisting in the solution, the resulting photoluminescent intensities of terbium are almost one order of magnitude weaker compared to those of the dispersed Tb-ZrBTB-120; this finding indicates that the energy transfer from the BTB linkers to the adjacent installed terbium is much more effective than that to the dissolved terbium ions.

336 | *Mol. Syst. Des. Eng.*, 2023, **8**, 330–340

This journal is © The Royal Society of Chemistry and IChemE 2023

The chemical stability of Tb-ZrBTB-120 in the environment for photoluminescence tests was then evaluated. As shown in Fig. S9,† Tb-ZrBTB-120 can well preserve its crystallinity after immersion in the cosolvent used for photoluminescence tests for 1 h. Furthermore, the photoluminescent intensity of Tb-ZrBTB-120 dispersed in the water–ethanol cosolvent (0.2 mg mL^{-1}) can stills remain 97% of its initial value after being dispersed for 50 min (Fig. S10(a) and (c)†). The Tb-ZrBTB-120 solid after being immersed in the cosolvent for 1 h was also collected, washed, and subjected to ICP-OES measurements, and the terbium loading of the sample barely changed (3.0 terbium on each hexa-zirconium node). All findings here indicate the chemical stability of Tb-ZrBTB-120 in the water–ethanol (1 : 1) cosolvent. On the other hand, when pure water was used to disperse Tb-ZrBTB-120, the photoluminescence decays to 67% of its initial value after 50 min (Fig. S10(b) and (d)†), and from ICP-OES, the solid after exposure to pure water for 1 h possesses a much lower terbium loading of 2.0 Tb per node. This result indicates that significant leaching of terbium ions from the material occurs in pure water. In addition, the emission of Tb-ZrBTB-120 measured in the cosolvent has much stronger intensities than that measured in pure water (see Fig. S10(a) and (b)†), which may be attributed to the quenching effect of high-energy vibrators, *i.e.*, H$_2$O here, coordinated on the terbium ions.[67] These findings strongly support the use of water–ethanol cosolvent as the working environment for all following photoluminescence tests. Cosolvents with various ethanol-to-water ratios were also tested, and the PXRD data in Fig. S9† suggest that the material is structurally stable in all of them. From ICP-OES data, the terbium loadings of the samples after immersion in the cosolvents with ethanol-to-water ratios of 3 : 1 and 1 : 3 are 3.3 and 2.6 terbium per hexa-zirconium node, respectively.

For photoluminescence nitrite detection, Tb-ZrBTB-120 was first dispersed in ethanol, and the suspension was mixed with the target aqueous sample containing nitrite. As shown in Fig. 7(a), the photoluminescent response from terbium significantly decreases as the concentration of nitrite increases. It is worth mentioning that the emission of BTB at 370 nm is fully independent of the concentration of nitrite, implying that the emission of BTB may be used as the internal standard for the sensing system toward ratiometric fluorescence detection. The Stern–Volmer equation was then applied to the photoluminescent intensities recorded at 543 nm, and the resulting plot is shown in Fig. 7(b). A good linearity between the relative intensity (I_0/I) and the concentration of nitrite can be achieved between 0.1 and 10 μM, with a Stern–Volmer constant (K_{sv}) of 472 000 M^{-1}. Furthermore, the limit of detection (LOD) was estimated to be 81.8 nM based on the signal-to-noise ratio of 3; the standard deviation for LOD calculation was estimated from six parallel photoluminescence tests without adding nitrite (Fig. S11†). Compared to other photoluminescent nitrite sensors reported previously, Tb-ZrBTB-120 exhibits a relatively low LOD (see Table S1†). After the exposure of Tb-
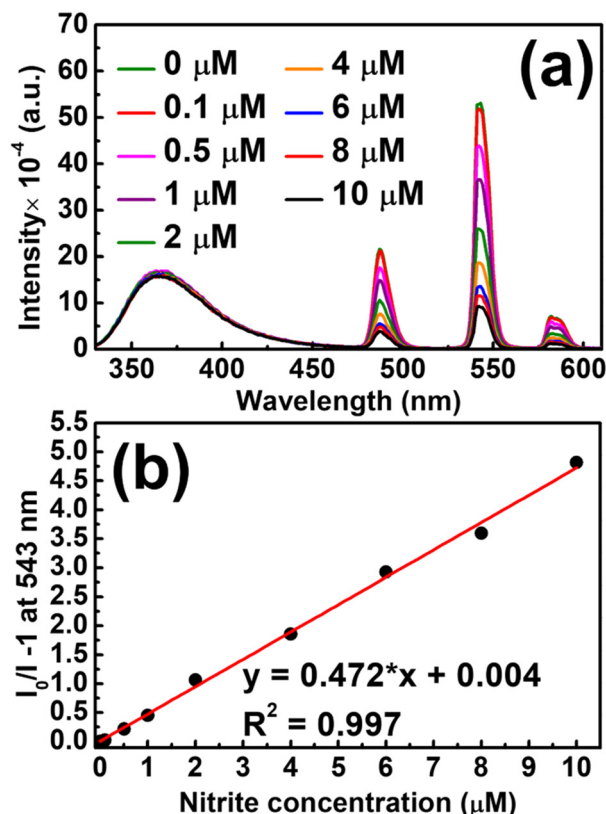

Fig. 7 (a) Emission spectra of Tb-ZrBTB-120 dispersed in the ethanol–water cosolvent (1 : 1) containing various concentrations of nitrite, measured under an excitation at 310 nm. (b) Stern–Volmer plot of Tb-ZrBTB-120 extracted from (a) at the wavelength of 543 nm. Concentration of Tb-ZrBTB-120 is 0.2 mg mL^{-1}.

ZrBTB-120 to the solution containing 10 μM of nitrite for 1 h, the crystallinity of the MOF can be fully preserved, suggesting the chemical stability of Tb-ZrBTB-120 in the sensing environment (Fig. S12†). In addition, the Tb-ZrBTB-120 material after exposure to nitrite was also subjected to FTIR and ICP-OES measurements. As shown in Fig. S13,† the characteristic peak of nitrite located at 1260 cm^{-1} is not present in the FTIR spectrum of Tb-ZrBTB-120 after the immersion in the solution containing nitrite for 1 h followed by the successive washing steps.[68] This result indicates that the irreversible adsorption of nitrite in Tb-ZrBTB-120 did not occur during the sensing process. From ICP-OES analysis, the loading of terbium in Tb-ZrBTB-120 after the immersion in the nitrite solution for 1 h was found to be 2.9 Tb per node, which is almost the same as the terbium loading in Tb-ZrBTB-120 after the immersion in the same ethanol–water cosolvent without adding nitrite (3.0 Tb per node). This observation indicates that the leaching of terbium caused by nitrite is negligible during the sensing process.

The selectivity of the Tb-ZrBTB-120-based nitrite sensor was then evaluated by adding several potential ionic interferents that are commonly present in environmental wastewater samples.[69,70] As shown in Fig. 8, the photoluminescence quenching behavior of Tb-ZrBTB-120 is
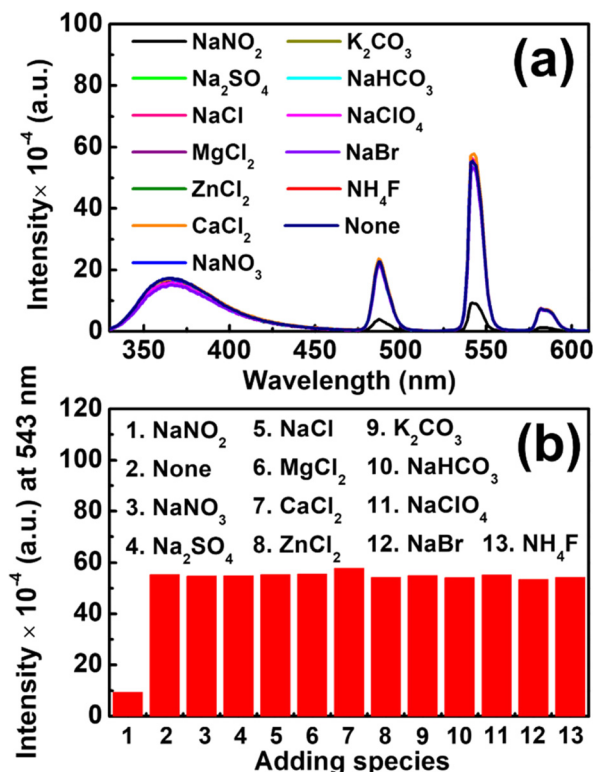
Fig. 8 (a) Emission spectra of Tb-ZrBTB-120 dispersed in the ethanol–water cosolvent (1:1) containing different chemicals, measured under an excitation at 310 nm. Concentrations of sodium nitrite and all interferents are 10 μM, and the concentration of Tb-ZrBTB-120 is 0.2 mg mL⁻¹. (b) Intensities at 543 nm extracted from (a).

highly selective toward nitrite, suggesting the applicability of Tb-ZrBTB-120 to detect nitrite in aqueous samples.

Conclusions

The installation of spatially dispersed terbium ions on the nodes of a water-stable 2D Zr-MOF, ZrBTB, can be successfully achieved by a solution-phase post-synthetic modification (PSM) process, and the loading of incorporated terbium ions can be modulated by simply changing the temperature of PSM. By installing terbium at 40 °C, 80 °C, and 120 °C, the loadings of terbium in the Zr-MOF were found to be 0.8, 2.0, and 3.3 Tb per node, respectively. The crystallinity, morphology, and major porosity of the MOF can be preserved after the installation of terbium at various temperatures, and uniform distributions of terbium can be found on the 2D MOF sheets. The obtained Tb-installed ZrBTB synthesized at 120 °C contains both Tb^{3+} and Tb^{4+}, and it was found that the metal substitution between terbium and the hexa-zirconium nodes did not occur. With the help of the BTB linkers to facilitate energy transfer to the installed Tb sites in the 2D MOF, the photoluminescent response of terbium can be significantly amplified, and its intensity is highly tunable by adjusting the temperature for installing terbium. Tb-ZrBTB-120 shows high chemical stability in the ethanol–water cosolvent and can be utilized in turn-off

photoluminescence nitrite detection for aqueous samples. The resulting nitrite sensor achieves a Stern–Volmer constant of 472 000 M^{-1}, a low LOD of 81.8 nm, and good selectivity against other common ionic interferents. The findings here open up opportunities for utilizing such water-stable and porous 2D Zr-MOF sheets as a platform to post-synthetically install various luminescent metal ions with tunable loadings for a range of sensing and photocatalytic applications in future studies.

Conflicts of interest

There are no conflicts to declare.

Acknowledgements

Notes and references

1 M. D. Allendorf, C. A. Bauer, R. K. Bhakta and R. J. Houk, *Chem. Soc. Rev.*, 2009, **38**, 1330–1352.

2 Y. Cui, Y. Yue, G. Qian and B. Chen, *Chem. Rev.*, 2012, **112**, 1126–1162.

3 A. J. Howarth, Y. Liu, P. Li, Z. Li, T. C. Wang, J. T. Hupp and O. K. Farha, *Nat. Rev. Mater.*, 2016, **1**, 15018.

4 H. Furukawa, K. E. Cordova, M. O'Keeffe and O. M. Yaghi, *Science*, 2013, **341**, 1230444.

5 Y. Zhang, S. Yuan, G. Day, X. Wang, X. Yang and H.-C. Zhou, *Coord. Chem. Rev.*, 2018, **354**, 28–45.

6 T. Zhang and W. Lin, *Chem. Soc. Rev.*, 2014, **43**, 5982–5993.

7 W. P. Lustig, S. Mukherjee, N. D. Rudd, A. V. Desai, J. Li and S. K. Ghosh, *Chem. Soc. Rev.*, 2017, **46**, 3242–3285.

8 J. Heine and K. Muller-Buschbaum, *Chem. Soc. Rev.*, 2013, **42**, 9232–9242.

9 F. A. Paz, J. Klinowski, S. M. Vilela, J. P. Tome, J. A. Cavaleiro and J. Rocha, *Chem. Soc. Rev.*, 2012, **41**, 1088–1110.

10 T. K. Kim, J. H. Lee, D. Moon and H. R. Moon, *Inorg. Chem.*, 2013, **52**, 589–595.

11 J. Della Rocca, D. Liu and W. Lin, *Acc. Chem. Res.*, 2011, **44**, 957–968.

12 M. C. So, G. P. Wiederrecht, J. E. Mondloch, J. T. Hupp and O. K. Farha, *Chem. Commun.*, 2015, **51**, 3501–3510.

13 X. Li, J. Yu, D. J. Gosztola, H. C. Fry and P. Deria, *J. Am. Chem. Soc.*, 2019, **141**, 16849–16857.

338 | *Mol. Syst. Des. Eng.*, 2023, **8**, 330–340

This journal is © The Royal Society of Chemistry and IChemE 2023

14 J. Rocha, L. D. Carlos, F. A. Paz and D. Ananias, *Chem. Soc. Rev.*, 2011, **40**, 926–940.

15 P. Mahata, S. K. Mondal, D. K. Singha and P. Majee, *Dalton Trans.*, 2017, **46**, 301–328.

16 Z. Liu, W. He and Z. Guo, *Chem. Soc. Rev.*, 2013, **42**, 1568–1600.

17 S. V. Eliseeva and J. C. Bunzli, *Chem. Soc. Rev.*, 2010, **39**, 189–227.

18 J. C. Bunzli and C. Piguet, *Chem. Soc. Rev.*, 2005, **34**, 1048–1077.

19 K. Binnemans, *Chem. Rev.*, 2009, **109**, 4283–4374.

20 X. Wang, L. Yue, P. Zhou, L. Fan and Y. He, *Inorg. Chem.*, 2021, **60**, 17249–17257.

21 Q. Yao, A. Bermejo Gómez, J. Su, V. Pascanu, Y. Yun, H. Zheng, H. Chen, L. Liu, H. N. Abdelhamid, B. Martín-Matute and X. Zou, *Chem. Mater.*, 2015, **27**, 5332–5339.

22 M. Tian, J. Zheng, J. Xue, X. Pan, D. Zhou, Q. Yao, Y. Li, W. Duan, J. Su and X. Huang, *Dalton Trans.*, 2021, **50**, 17785–17791.

23 S. M. Cohen, *J. Am. Chem. Soc.*, 2017, **139**, 2855–2863.

24 T. Islamoglu, S. Goswami, Z. Li, A. J. Howarth, O. K. Farha and J. T. Hupp, *Acc. Chem. Res.*, 2017, **50**, 805–813.

25 A. Carné-Sánchez, J. Albalad, T. Grancha, I. Imaz, J. Juanhuix, P. Larpent, S. Furukawa and D. Maspoch, *J. Am. Chem. Soc.*, 2019, **141**, 4094–4102.

26 B. Yan, *Acc. Chem. Res.*, 2017, **50**, 2789–2798.

27 Y. Shu, Q. Ye, T. Dai, Q. Xu and X. Hu, *ACS Sens.*, 2021, **6**, 641–658.

28 N. C. Burtch, H. Jasuja and K. S. Walton, *Chem. Rev.*, 2014, **114**, 10575–10612.

29 S. Pal, S.-S. Yu and C.-W. Kung, *Chemosensors*, 2021, **9**, 306.

30 S. Yuan, J. S. Qin, C. T. Lollar and H. C. Zhou, *ACS Cent. Sci.*, 2018, **4**, 440–450.

31 V. Bon, I. Senkovska, I. A. Baburin and S. Kaskel, *Cryst. Growth Des.*, 2013, **13**, 1231–1237.

32 J. H. Cavka, S. Jakobsen, U. Olsbye, N. Guillou, C. Lamberti, S. Bordiga and K. P. Lillerud, *J. Am. Chem. Soc.*, 2008, **130**, 13850–13851.

33 J. Zhang, S. B. Peh, J. Wang, Y. Du, S. Xi, J. Dong, A. Karmakar, Y. Ying, Y. Wang and D. Zhao, *Chem. Commun.*, 2019, **55**, 4727–4730.

34 K. Yi, H. Li, X. Zhang and L. Zhang, *Inorg. Chem.*, 2021, **60**, 3172–3180.

35 H. S. Jena, A. M. Kaczmarek, C. Krishnaraj, X. Feng, K. Vijayvergia, H. Yildirim, S.-N. Zhao, R. Van Deun and P. V. Der Voort, *Cryst. Growth Des.*, 2019, **19**, 6339–6350.

36 L. Li, S. Shen, W. Ai, S. Song, Y. Bai and H. Liu, *Sens. Actuators, B*, 2018, **267**, 542–548.

37 D. J. Ashworth and J. A. Foster, *J. Mater. Chem. A*, 2018, **6**, 16292–16307.

38 H. Yuan, G. Liu, Z. Qiao, N. Li, P. J. S. Buenconsejo, S. Xi, A. Karmakar, M. Li, H. Cai, S. J. Pennycook and D. Zhao, *Adv. Mater.*, 2021, **33**, 2101257.

39 X. Feng, Y. Song and W. Lin, *J. Am. Chem. Soc.*, 2021, **143**, 8184–8192.

40 Y. Xiao, J. Liu, J. Leng, Z. Yin, Y. Yin, F. Zhang, C. Sun and S. Jin, *ACS Energy Lett.*, 2022, **7**, 2323–2330.

41 L. Cao, Z. Lin, W. Shi, Z. Wang, C. Zhang, X. Hu, C. Wang and W. Lin, *J. Am. Chem. Soc.*, 2017, **139**, 7020–7029.

42 Z. Li, D. Zhan, A. Saeed, N. Zhao, J. Wang, W. Xu and J. Liu, *Dalton Trans.*, 2021, **50**, 8540–8548.

43 H. Xu, J. Gao, X. Qian, J. Wang, H. He, Y. Cui, Y. Yang, Z. Wang and G. Qian, *J. Mater. Chem. A*, 2016, **4**, 10900–10905.

44 L. Feng, Y. Qiu, Q.-H. Guo, Z. Chen, J. S. Seale, K. He, H. Wu, Y. Feng, O. K. Farha and R. D. Astumian, *Science*, 2021, **374**, 1215–1221.

45 J. Ma, A. G. Wong-Foy and A. J. Matzger, *Inorg. Chem.*, 2015, **54**, 4591–4593.

46 Z. Wang, Y. Liu, Z. Wang, L. Cao, Y. Zhao, C. Wang and W. Lin, *Chem. Commun.*, 2017, **53**, 9356–9359.

47 H. Min, Z. Han, M. Wang, Y. Li, T. Zhou, W. Shi and P. Cheng, *Inorg. Chem. Front.*, 2020, **7**, 3379–3385.

48 J.-X. Wu and B. Yan, *Ind. Eng. Chem. Res.*, 2018, **57**, 7105–7111.

49 H. Xu, H.-C. Hu, C.-S. Cao and B. Zhao, *Inorg. Chem.*, 2015, **54**, 4585–4587.

50 Y. Wang, L. Feng, J. Pang, J. Li, N. Huang, G. S. Day, L. Cheng, H. F. Drake, Y. Wang, C. Lollar, J. Qin, Z. Gu, T. Lu, S. Yuan and H. C. Zhou, *Adv. Sci.*, 2019, **6**, 1802059.

51 Z. Lu, J. Liu, X. Zhang, Y. Liao, R. Wang, K. Zhang, J. Lyu, O. K. Farha and J. T. Hupp, *J. Am. Chem. Soc.*, 2020, **142**, 21110–21121.

52 C.-H. Chuang, J.-H. Li, Y.-C. Chen, Y.-S. Wang and C.-W. Kung, *J. Phys. Chem. C*, 2020, **124**, 20854–20863.

53 H. Noh, Y. Cui, A. W. Peters, D. R. Pahls, M. A. Ortuno, N. A. Vermeulen, C. J. Cramer, L. Gagliardi, J. T. Hupp and O. K. Farha, *J. Am. Chem. Soc.*, 2016, **138**, 14720–14726.

54 C.-H. Shen, Y.-H. Chen, Y.-C. Wang, T.-E. Chang, Y.-L. Chen and C.-W. Kung, *Phys. Chem. Chem. Phys.*, 2022, **24**, 9855–9865.

55 Z. Hu, E. M. Mahdi, Y. Peng, Y. Qian, B. Zhang, N. Yan, D. Yuan, J.-C. Tan and D. Zhao, *J. Mater. Chem. A*, 2017, **5**, 8954–8963.

56 J. Zhao, R. Chen, J. Huang, F. Wang, C. A. Tao and J. Wang, *ACS Appl. Mater. Interfaces*, 2021, **13**, 40863–40871.

57 Y. Li and R. T. Yang, *Langmuir*, 2007, **23**, 12937–12944.

58 P. Chen, Y. Liu, X. Hu, X. Liu, E.-M. You, X. Qian, J. Chen, L. Xiao, L. Cao, X. Peng, Z. Zeng, Y. Jiang, S.-Y. Ding, H. Liao, Z. Wang, D. Zhou and C. Wang, *Nano Res.*, 2020, **13**, 3151–3156.

59 Y. Wang, L. Li, L. Yan, X. Gu, P. Dai, D. Liu, J. G. Bell, G. Zhao, X. Zhao and K. M. Thomas, *Chem. Mater.*, 2018, **30**, 3048–3059.

60 K. Chen, H. Gao, D. Wang, X. Li, D. Wang and W. U. Khan, *RSC Adv.*, 2018, **8**, 9287–9292.

61 Y. S. Wang, Y. C. Chen, J. H. Li and C. W. Kung, *Eur. J. Inorg. Chem.*, 2019, **2019**, 3036–3044.

62 E. J. Little Jr and M. M. Jones, *J. Chem. Educ.*, 1960, **37**, 231.

63 M. Kim, J. F. Cahill, H. Fei, K. A. Prather and S. M. Cohen, *J. Am. Chem. Soc.*, 2012, **134**, 18082–18088.

64 M. Lammert, C. Glißmann and N. Stock, *Dalton Trans.*, 2017, **46**, 2425–2429.

65 P. Deria, J. E. Mondloch, E. Tylianakis, P. Ghosh, W. Bury, R. Q. Snurr, J. T. Hupp and O. K. Farha, *J. Am. Chem. Soc.*, 2013, **135**, 16801–16804.

66 S.-L. Zhong, R. Xu, L.-F. Zhang, W.-G. Qu, G.-Q. Gao, X.-L. Wu and A.-W. Xu, *J. Mater. Chem. A*, 2011, **21**, 16574–16580.

67 S. A. Younis, N. Bhardwaj, S. K. Bhardwaj, K.-H. Kim and A. Deep, *Coord. Chem. Rev.*, 2021, **429**, 213620.

68 D. F. Sava Gallis, D. J. Vogel, G. A. Vincent, J. M. Rimsza and T. M. Nenoff, *ACS Appl. Mater. Interfaces*, 2019, **11**, 43270–43277.

69 Y.-C. Wang, Y.-C. Chen, W.-S. Chuang, J.-H. Li, Y.-S. Wang, C.-H. Chuang, C.-Y. Chen and C.-W. Kung, *ACS Appl. Nano Mater.*, 2020, **3**, 9440–9448.

70 T.-E. Chang, C.-H. Chuang and C.-W. Kung, *Electrochem. Commun.*, 2021, **122**, 106899.